Materials Today Bio 28 (2024) 101240

Contents lists available at ScienceDirect

Materials Today Bio

journal homepage: www.journals.elsevier.com/materials-today-bio

In vivo targeted-imaging of mitochondrial acidification in an aristolochic acid I-induced nephrotoxicity mouse model by a fluorescent/photoacoustic bimodal probe

Li Xu [a,b,1], Li Chen [a,1], Hongwen Liu [c,d,*], Xingwang Chen [c], Shenghang Zhang [a,**]

[a] Fujian Key Laboratory of Aptamers Technology, Fuzhou General Clinical Medical School (the 900th Hospital), Fujian Medical University, Fuzhou, 350025108, China
[b] Department of Anesthesiology and Surgical Intensive Care Unit, Xinhua Hospital, School of Medicine and School of Biomedical Engineering, Shanghai Jiao Tong University, Shanghai, 200092, China
[c] College of Chemistry and Chemical Engineering, Hunan Normal University, Changsha, 410081, China
[d] The School of Chemistry and Chemical Engineering, Henan Normal University, Xinxiang, Henan, 453007, China

ARTICLE INFO

Keywords:
Aristolochic acid
Nephrotoxicity
In vivo mitophagy
Fluorescent imaging
Photoacoustic imaging

ABSTRACT

Aristolochic acid I (AAI), a natural compound in aristolochia type Chinese medicinal herb, is generally acknowledged to have nephrotoxicity, which may be associated with mitophagy. Mitophagy is a cellular process with important functions that drive AAI-induced renal injury. Mitochondrial pH is currently measured by fluorescent probes in cell culture, but existing probes do not allow for in situ imaging of AAI-induced mitophagy in vivo. We developed a ratiometric fluorescent/PA dual-modal probe with a silicon rhodamine fluorophore and a pH-sensitive hemicyanine dye covalently linked via a short chain to obtain a FRET type probe. The probe was used to measure AAI-mediated mitochondrial acidification in live cells and in vivo. The Förster resonance energy transfer (FRET)-mediated ratiometric and bimodal method can efficiently eliminate signal variability associated with the commonly used one-emission and single detection mode by ratiometric two channels of the donor and acceptor. The probe has good water-solubility and low molecular weight with two positively charged, facilitating its precise targeting into renal mitochondria, where the fluorescent/PA changes in response to mitochondrial acidification, enabling dynamic and semi-quantitative mapping of subtle changes in mitochondrial pH in AAI-induced nephrotoxicity mouse model for the first time. Also, the joint use of L-carnitine could mitigate the mitophagy in AAI-induced nephrotoxicity.

1. Introduction

Aristolochic acid I (AAI), a naturally occurring compound in aristolochia type Chinese medicinal herb, is generally acknowledged to have hepatotoxicity and nephrotoxicity [1], which may associate with autophagy [2]. In recent years, with the deepening of studies on aristolochic acid, researchers have found that AAI has strong hepatotoxicity and nephrotoxicity. Improper utilization of AA can cause severe liver and kidney disease. Mitochondria, the main places where reactive oxygen species (ROS) are produced, are more tend to suffer from the increase cellular oxidative stress induced by AAI, followed with mitochondrial damage and subsequent autophagy, during the AAI induced renal and hepatic injury [3]. Mitochondria play a large role in autophagy, which is also known as mitophagy, a crucial biological process that plays a central role in regulating mitochondrial activity and controlling metabolic quality during cell metabolism [4]. Relevant studies have indicated that moderate mitophagy can increase cell tolerance, clear senescent or damaged organelles, facilitate cell survival, and exerts a protective effect [5]. While, excessive mitophagy can lead to overdone degradation of related proteins and organelles, resulting in the death of numerous autophagic cells, aggravating cell injury and accelerating cell death [6]. Currently, some studies have pointed out that the acute phase of AAI-induced nephropathy is associated with induction of mitophagy based on methods such as proteomics [7,8]. However, current methods are failed to providing real-time and in situ information of this biological event in vivo.

* Corresponding author. College of Chemistry and Chemical Engineering, Hunan Normal University, Changsha, 410081, China.
** Corresponding author.
E-mail addresses: liuhongwen@hnu.edu.cn (H. Liu), fzzyyzsh@126.com (S. Zhang).
[1] L. Xu and L. Chen contributed equally to this work.

https://doi.org/10.1016/j.mtbio.2024.101240
Received 10 July 2024; Received in revised form 4 September 2024; Accepted 10 September 2024
Available online 11 September 2024

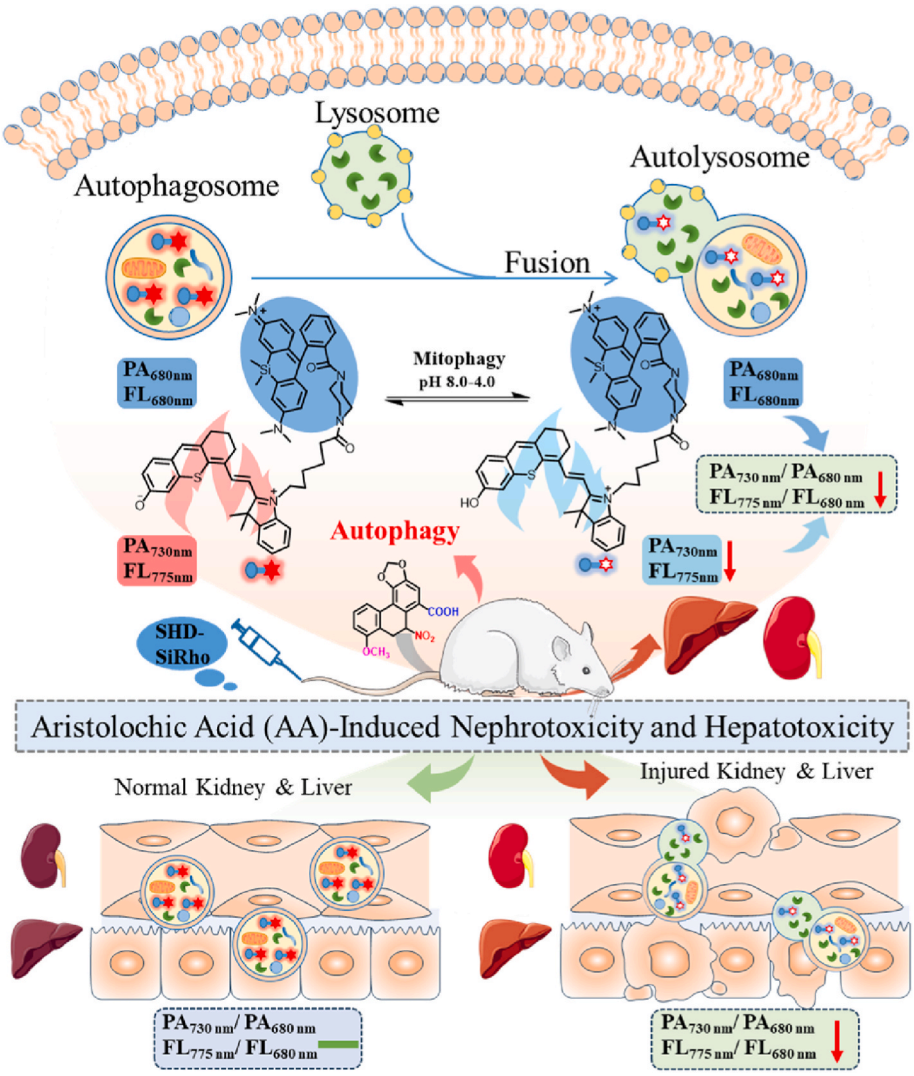

Scheme 1. Schematic illustration of the design of a FRET-Based molecular probe SHD-SiRho, to enable the ratiometric fluorescent (FL) and photoacoustic (PA) dual-modal imaging of mitochondrial acidification in an aristolochic acid I-induced organ injury mouse model.

Fluorescence imaging technology can fulfill the needs of real-time monitoring the autophagy via using autophagy biomarker-activable molecule probe [9–11]. In the past years, mitophagy, within living cells, have been well revealed due to development of the selective biomarker and sensitive fluorescent probes for real-time confocal fluorescence monitoring the phenomenon in living cells. However, the mitophagy within tissues and whole organisms exhibit substantial complexities beyond those found in cell culture studies, but remaining hardly studied [12]. Currently, the study of in vivo mitophagy has been hindered by the lack of "tissue and mitochondria dual targeted" molecule probes for real-time monitoring this event in specific organisms. For monitoring in vivo mitophagy in AAI-induced nephropathy, it requires the molecule probes first enrich in the renal tissues then anchor in renal cells' mitochondria, so as to achieve the monitoring mitophagy in kidneys. However, due to the uncertainty of in vivo distribution of molecule probes [13–15], the in vivo mitophagy imaging remains big challenge. Based on the renal metabolizing hydrophilic small molecules with molecular weight lower than 40 kDa, or small nanoparticles hydrodynamic diameters below the kidney filtration threshold (5.5 nm), a few of fluorescent ultrasmall gold nanoparticles, silica Cornell dots, quantum dots, and a series of hydrophilic macromolecule probes have been developed, which could stay in the kidneys for a period of time, to achieve bioimaging of kidney dysfunction [16–25]. However, such hydrophilic macromolecule probes mainly achieve kidney clearance by modifying hydrophilic groups, such as PEG, cyclodextrin, and polypeptide, which make them internalized by kidney cells through the endocytic pathway and be detained in the lysosomes. Thus, the existing strategies for designing renal-targeted imaging probes are not suitable for constructing molecule probe for monitoring in vivo mitophagy in AAI-induced nephropathy.

Organic cation transporters (OTCs)-mediated cellular uptake emerges as a feasible strategy for constructing molecule probe for monitoring biological events in kidneys [26–31]. OCT is mainly distributed on the basal membrane side of renal proximal tubular epithelial cells, transporting heterocyclic weakly alkaline substances through OC^{+}/H^{+} exchange, including endogenous substances (such as polyhexylamine, adrenaline, and choline) and weakly alkaline drugs [27]. Among them, Oct2 is the most widely expressed organic cation transporter on the basal lateral side of the kidney, mediating the transport of cisplatin from the blood to proximal tubular epithelial cells, followed with cisplatin-induced renal injury [32]. Thus, cationic molecule probes with good water solubility may actively enrich in the kidneys with the help of OTCs, and further localize in mitochondria of renal cells via strong interaction with mitochondrial membranes. In order to detect mitophagy in AAI induced renal injury, monitoring the dynamic changes in pH was chosen preferentially as the pH changes from 8.0 to

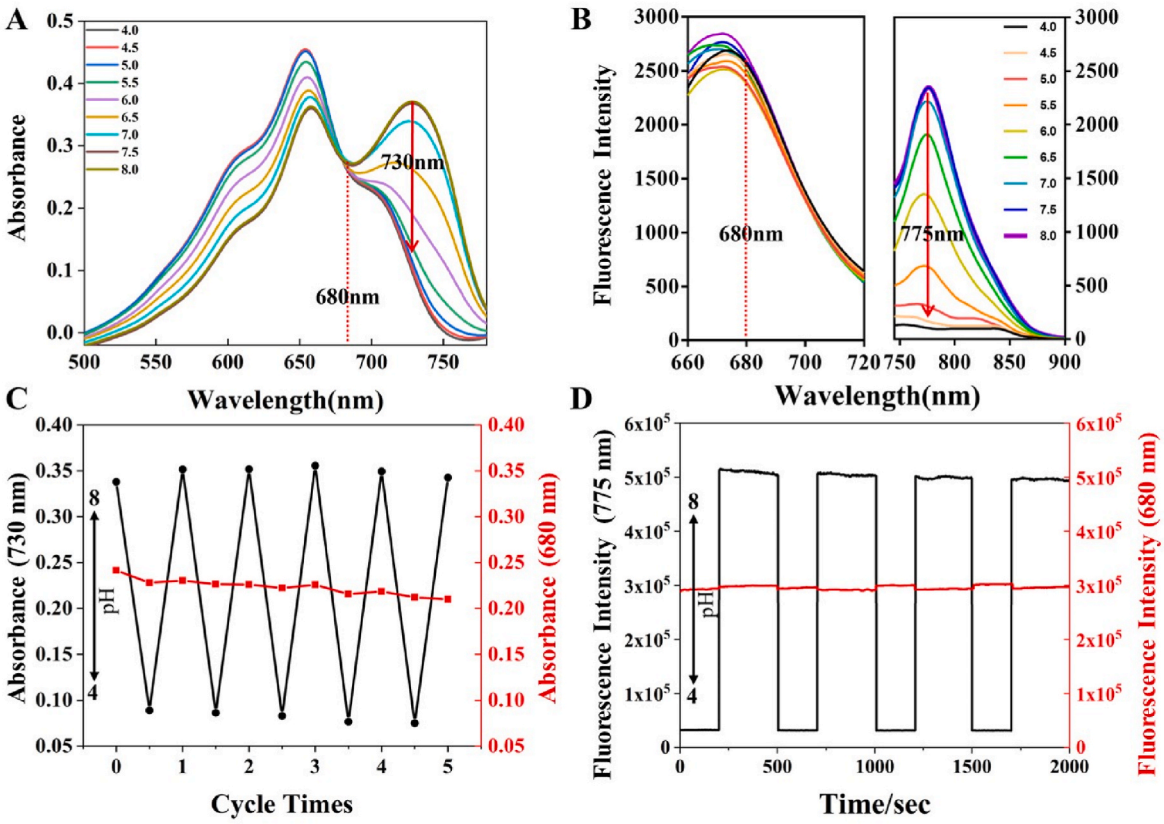

Fig. 1. The in vitro spectral testing of 5 μM SHD-SiRho in buffered solution (PBS/EtOH = 2:1, v/v, 10 mM, pH = 4.0–8.0). (A) Absorption and (B) fluorescent emission spectra of SHD-SiRho (5 μM) with different pH in aqueous solution at 37 °C. (C) Absorbance intensity A_{730nm} and A_{680nm} of SHD-SiRho with reversible cycling at pH = 4.0–8.0. (D) Fluorescence intensity FL_{775nm} and FL_{680nm} of SHD-SiRho with reversible cycling at pH = 4.0–8.0. λ_{ex} = 640 nm or 730 nm.

about 4.0 during the mitophagy process. Most pH repones fluorescent probes are based on the protonation and deprotonation of hydroxyl or amino groups [33], which are generally reversible endowing dynamic monitoring the pH change. And the *pKa* value of the probes can be kept within the range of 8.0 to 4.0 through molecular engineering, making them suitable for detect mitophagy. Indeed, great progress has been made in pH fluorescent probes [34–40], some of them were applied for pH measurement in tumors [35–38]. However, mitochondrial pH is generally measured by fluorescent probes in cell culture, but existing probes do not allow for visualizing mitophagy in AAI induced renal injury due to the inability of accumulation in the kidneys. On the other hand, the in vivo determination of pH using fluorescence imaging may also be interfered by some influences such as limited light penetration depth, background fluorescence, as well as possible quenching of fluorescence in the complicated biological issues. The aforementioned issues can be addressed by employing fluorescent and photoacoustic (PA) bimodal imaging. PA imaging relies on absorbance of light and emission of ultrasound signals, exhibits greatly enhanced tissue penetration depth and better in vivo spatial resolution compared to conventional optical imaging techniques [41]. Moreover, molecule probes depend on single channel signal change for in vivo imaging, which tends to be easily interfered with various environmental factors, making it less probable for dynamic monitoring of mitochondrial acidification in deep tissues [42–44]. To date, no pH probes have been reported to demonstrate good mitochondrial localization ability in kidneys, low background signals, minimized signal variability, and high imaging resolution simultaneously.

Herein, we developed a kidney and mitochondria dual targeted, pH response molecule probe with ratiometric near-infrared (NIR) fluorescent/PA signal for in situ and dual channel and dual modal imaging of mitophagy in AAI induced renal injury. The probe (SHD-SiRho) consists of two NIR dyes, one is a silicon rhodamine (SiRho) fluorophore with good water-solubility and intense fluorescence, and the other is a pH-sensitive hemicyanine fluorophore (SHD), meanwhile both possess high molar extinction coefficient endowing good fluorescent/PA dual modal imaging performance (Scheme 1). These two dyes are linked via short chains to obtain a Förster resonance energy transfer (FRET) type probe. The FRET-mediated ratiometric method can efficiently eliminate signal variability associated with the commonly used one-channel detection by ratiometric two signal channels of the donor and acceptor. With the decrease of pH from 8.0 to 4.0 in the solution, a gradual decrease in the probe's absorbance peak at 730 nm, resulting in a "turn-off" PA signal at 730 nm and a gradual decrease in fluorescence at 780 nm. Conversely, the PA signal at 680 nm and fluorescence at 680 nm from the reserved signal of SiRho remain relatively constant, which are minimal influence form pH changes acting as internal reference signals for fluorescent/PA imaging. Moreover, the probe molecule has good water-solubility and small molecular weight with two positively charged, facilitating its precise targeting into renal mitochondria. With such a FRET-based probe, the in situ and real-time monitoring of the process of mitophagy in AAI-induced renal injury mouse model was achieved by fluorescent/PA dual modal and ratiometric imaging. This work provides a novel tool for visualization of in vivo mitophagy and promoting the mechanism study of AAI-induced renal injury.

2. Results and discussion

Optimized Design and Synthesis of SHD-SiRho. There is currently an insufficient methodology to confirm the association between AAI-induced nephrotoxicity and mitophagy, thereby limiting the exploration of the underlying mechanisms of AAI nephrotoxicity. In order to detect mitophagy in AAI-induced renal injury, monitoring the dynamic

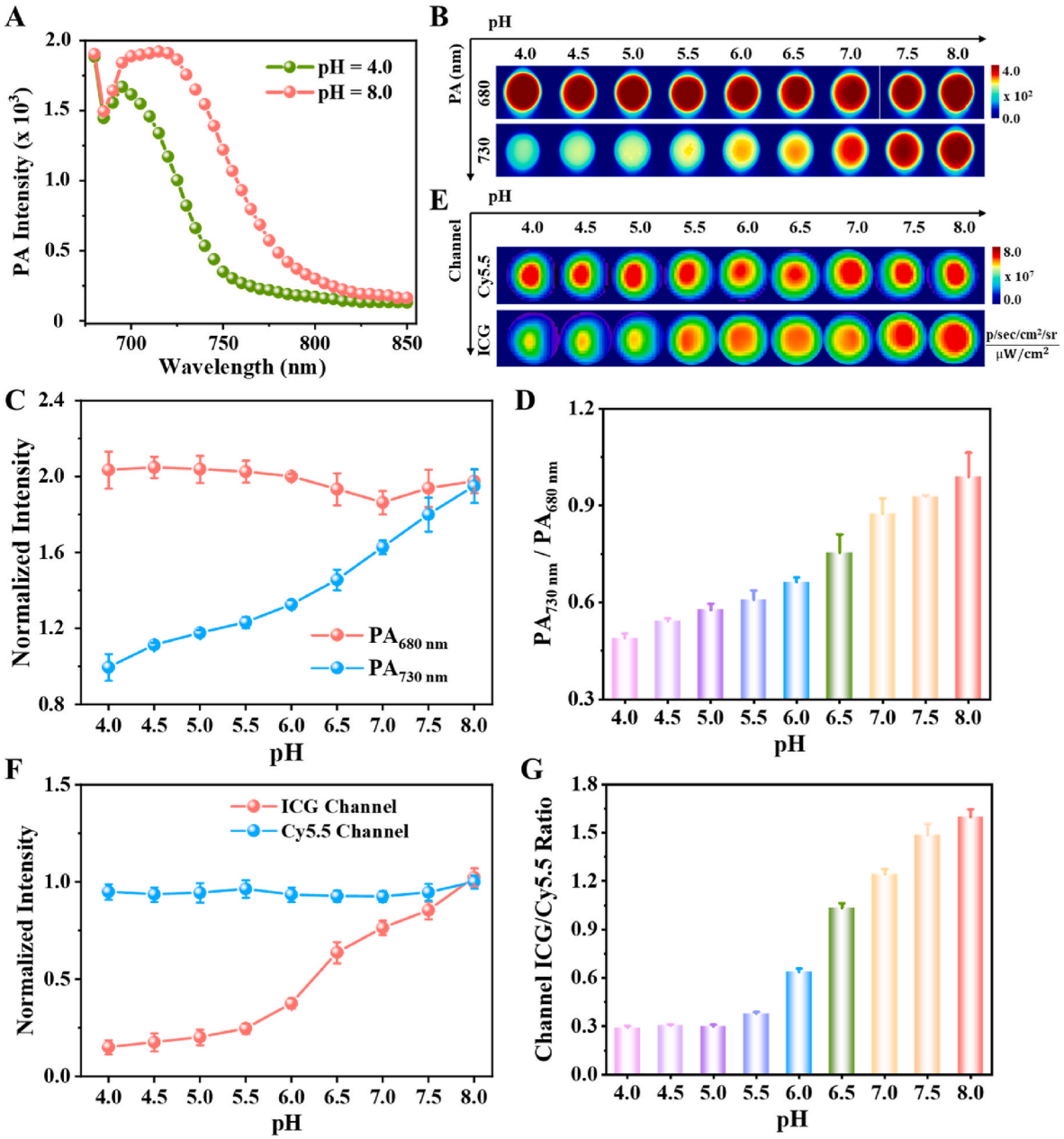

Fig. 2. The in vitro fluorescent/PA imaging of SHD-SiRho (5 μM) in buffered solution (PBS/EtOH = 2:1, v/v, 10 mM, pH = 4.0–8.0). (A) PA spectra of the 5 μM SHD-SiRho in buffered solution (PBS/EtOH = 2:1, v/v, 10 mM, pH = 4.0, pH = 8.0). (B) $PA_{680\ nm}$ and $PA_{730\ nm}$ images of SHD-SiRho toward pH in buffered solutions with different pH values. (C) $PA_{680\ nm}$ and $PA_{730\ nm}$ signals of SHD-SiRho toward pH = 4.0–8.0. (D) $PA_{730\ nm}/PA_{680\ nm}$ signal intensity ratios of SHD-SiRho based on PA imaging data in (B). (E) Fluorescence emission images of Cy5.5 and ICG channels of SHD-SiRho toward pH in buffered solutions with different pH values. (F) Fluorescent signals of SHD-SiRho at Cy5.5 channel and ICG channel toward pH = 4.0–8.0. (G) ICG channel/Cy5.5 channel signal intensity ratios of SHD-SiRho samples based on fluorescent imaging data in (E). λ_{ex} = 680 nm or 730 nm for PA imaging, and λ_{ex} = 640 nm, λ_{em} = 650–700 nm (Cy5.5 channel) and 750–800 nm (ICG channel) for fluorescent imaging.

changes in pH was chosen preferentially as the pH changes from 8.0 to about 4.0640 during the mitophagy process. However, currently mitochondria-anchored pH probes failed to achieve in situ imaging of mitochondrial acidification in an AAI-induced nephrotoxicity mouse model. Therefore, it is imperative to develop a molecular probe capable of targeting mitochondria and enriching in the kidneys for dynamical monitoring the changes in pH for investigating AAI-induced mitophagy. There are currently some strategies to achieve tissue-specific in vivo imaging of molecular probes, such as active targeting strategies [45–48], zwitterionic fluorophores [49], and structure-inherent targeting [50]. However, targeted imaing of mitophagy in kidneys remained challenge. Based on our previous experimental findings, the integration of silicon rhodamine and semi-cyanine dye had good renal metabolic ability [51], which may be concluded that cationic molecule probes with good water solubility may actively enrich in the kidneys with the help of OTCs. To ensure sensitive pH monitoring, we selected a hemicyanine (SHD) fluorophore with hydroxyl group [52], known for its good responsive behavior to pH, as the recognition part of our probe. Pre-experimental results indicated that the SHD fluorophore exhibited excellent pH responsiveness within the range of pH 4.0–8.0 (Figs. S1A and S1B). On the other hand, a FRET-based ratiometric imaging approach can further remarkably eliminate signal mutability related to the usually used single-channel detection by two signal bands of the acceptor and donor. So, we chose the Si-rhodamine (SiRho) fluorophore with excellent

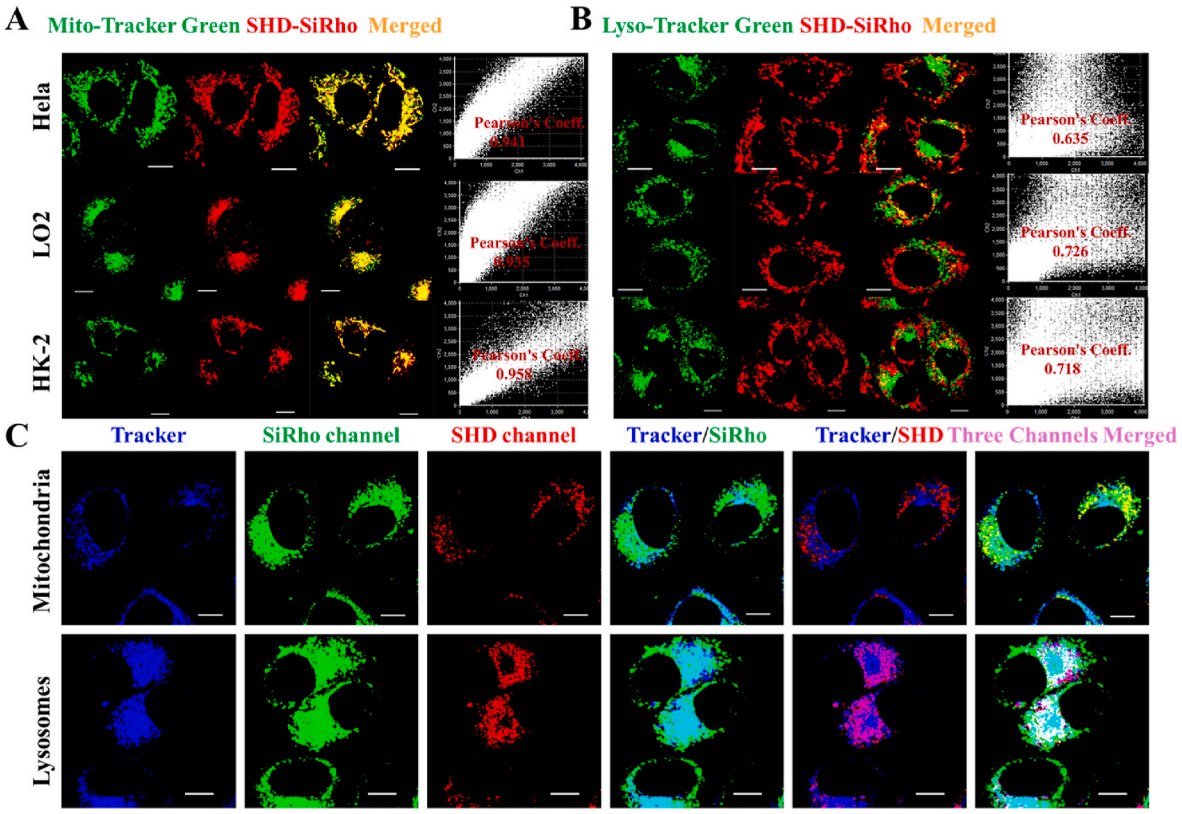

Fig. 3. Fluorescence imaging of subcellular localization of SHD-SiRho (2.5 μM). SHD-SiRho was incubated with HeLa, L-O2 and HK-2 cells at 37 °C for 6 h and then cells were incubated with MitoTracker® Green (A) or LysoTracker® Green (B) for another 10 min, respectively. (C) Fluorescent images of HeLa cells incubated with SHD-SiRho and then exposed under hypoxia (~0.1 % O_2) conditions for 6 h, then co-incubation with MitoTracker® Green or LysoTracker® Green, respectively for another 10 min before imaging. LysoTracker® Green, λ_{ex} = 488 nm, λ_{em} = 500–560 nm; MitoTracker® Green, λ_{ex} = 488 nm, λ_{em} = 500–560 nm; SHD-SiRho, λ_{ex} = 640 nm, λ_{em} = 660−700 nm for SiRho channel and λ_{em} = 720−780 nm for SHD channel; Scale bar: 10 μm.

photophysical characteristics as the donor to construct the FRET system [53]. The feasibility of FRET system was verified by density functional theory calculation (Scheme S2) and examining the spectral properties of the SHD and SiRho fluorophores. The fluorescence emission spectra of the FRET donor fluorophore SiRho and the UV–visible absorbance spectra of the acceptor fluorophore SHD exhibited significant overlap at both pH 4.0 and pH 8.0 in the PBS buffer solution, indicating efficient energy transfer between them and the consistent suppression efficiency of SiRho's fluorescence (Figs. S1C and S1D). Due to the high fluorescence brightness of SiRho fluorophore, a partial signal remains after FRET (FRET efficiency is calculated to be 35 %), while SiRho is not affected by pH, so this partial signal can be used as an internal reference signal (Fig. S2). As a sharp contrast, the receptor SHD of the FRET system is pH-sensitive covered the range of pH 4.0–8.0 with good reproduction and reversibility. Thus, taking advantage of the dual FRET and ICT mechanism, we designed and synthesized SHD-SiRho as a fluorescent/PA bimodal and dual ratio-metric pH probe, which enables targeted-imaging of mitochondrial acidification in an AAI-induced nephrotoxicity. The detailed reaction methods are shown in Scheme S1 in the Supporting Information, all the new compounds were confirmed by $^{1}H/^{13}C$ NMR and ESI-MS, and characterization diagrams were presented.

Spectral response of probe to different pH buffer solutions. After synthesizing the probe, we initially characterized the spectral properties in vitro to verify whether the probe can show strong pH-dependent behavior. The absorption spectrum of SHD-SiRho incubated within pH buffers ranged 4.0–8.0 revealed a significantly decreased absorbance peak at 730 nm, while a stable peak at 680 nm (Fig. 1A). The absorbance intensity at 680 nm and 730 nm align with the desired attributes of an internal reference ratio probe (Figs. S3A and B). Furthermore, by analyzing the absorbance at 730 nm under different pH conditions, we calculated the pK_a value of the probe to be 6.25, corresponding to the pH range associated with the autophagy process. A similar result was obtained in the fluorescence spectrum of Fig. 1B, which showed that the probe's pronounced pH dependence. In addition, under the excitation wavelength of 730 nm and 640 nm, we collected the fluorescence intensity of the SHD-SiRho at 775 nm and 680 nm at different concentrations of H^+ (pH 4.0 to pH 8.0) (Fig. 1B). Figs. S3C and S3D displayed the fluorescence intensity maps of the probe at 680 nm and 775 nm, with pH in the range of 4.0–8.0, under excitation at 640 nm and 730 nm, respectively. These results exhibited that SHD-SiRho is a novel ratiometric probe with an internal reference. Notably, such kind of ratiometric probe, in which one signal can particularly respond to the analyte of interest, and the other one is target-independent and acts as an internal reference, endows a fidelity and credible method for ratiometric sensing and imaging [54]. We also measured the reversible response of the SHD-SiRho to pH Fig. 1C and D illustrated that the SHD-SiRho reversibly responded to pH changes (pH 4.0 and pH 8.0) with significant absorbance or fluorescence changes at 730 nm and 775 nm, respectively. After five cycles, the probe exhibited minimal attenuation in absorbance at 730 nm and fluorescence at 775 nm, indicating its excellent reversible response to H^+. In addition, we also evaluated the stability of SHD-SiRho in Dulbecco's modified Eagle's medium (DMEM) and DPBS (12 h, 24 h and 28 h), which containing proteins or various ions (Fig. S4). The synchronized changes of absorbance and fluorescence at 730 nm and 775 nm confirmed the high stability of SHD-SiRho in buffer systems. The test results clearly demonstrated that the SHD-SiRho is sensitive and stable to pH detection in the process of protonation and deprotonation, regardless of influence of buffer systems. To sum up, the SHD-SiRho is capable of monitoring the dynamic process of mitophagy

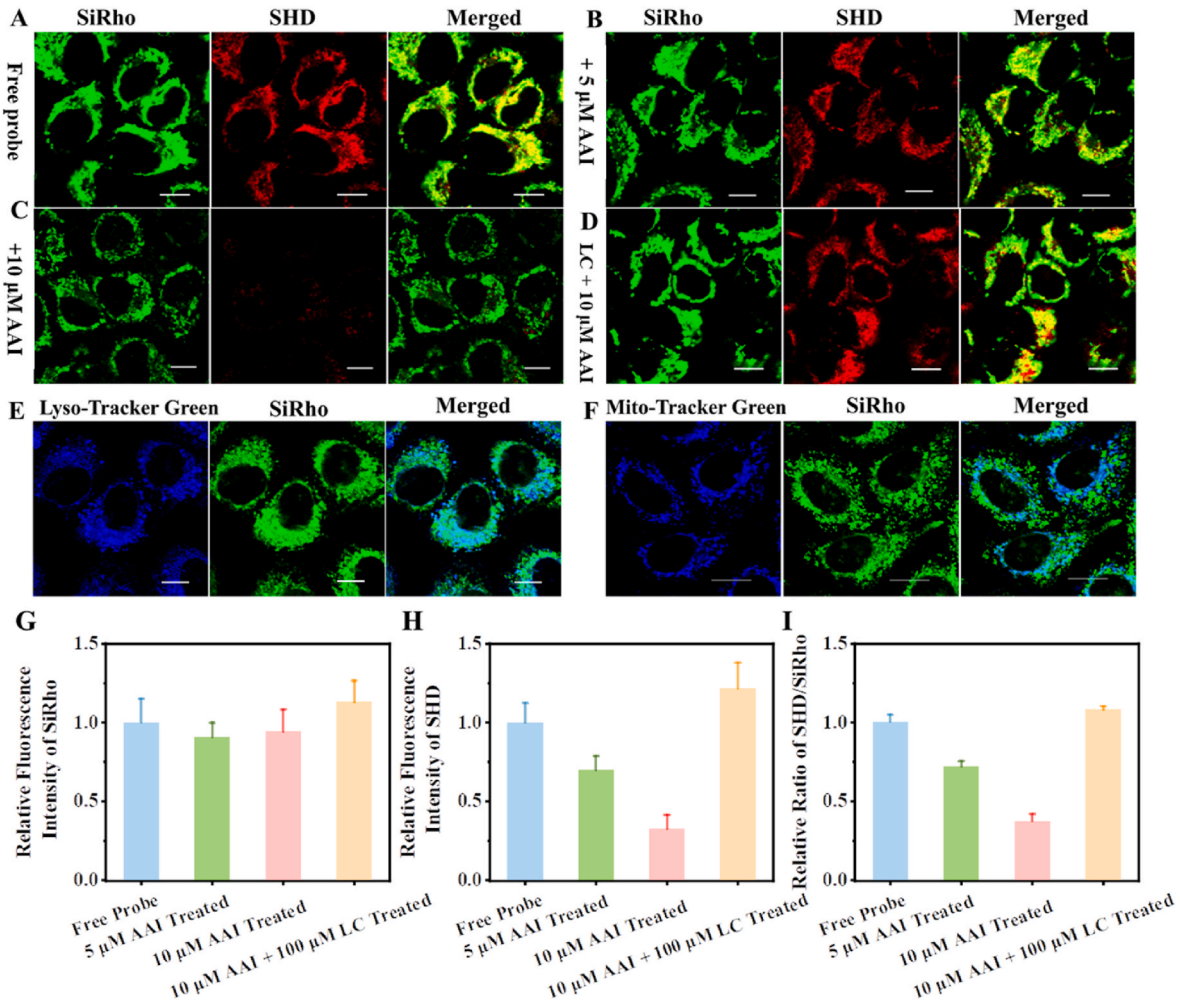

Fig. 4. Confocal fluorescence imaging of AAI-induced mitochondrial acidification in HK-2 cells. (A–C) HK-2 cells incubated with 0, 5, and 10 μM AAI, respectively, for 4 h, and then adding the probe SHD-SiRho (2.5 μM) for another 6 h. (D) HK-2 cells incubated with 10 μM AAI and 100 μM LC for 4 h, and then adding the probe SHD-SiRho (2.5 μM) for another 6 h. Colocalization images of SiRho with (E) Lyso-Tracker Green and (F) Mito-Tracker Green in HK-2 cells. (G) The relative fluorescence intensity of SiRho in HK-2 cells in each group. (H) The relative fluorescence intensity of SHD in HK-2 cells in each group. (I) The relative ratio of SHD/SiRho in HK-2 cells in each group. Green channel, SiRho imaging signal, λ_{ex} = 640 nm, λ_{em} = 650–700 nm; red channel, SHD imaging signal, λ_{ex} = 640 nm, λ_{em} = 720–780 nm, Lyso-Tracker Green imaging signal, λ_{ex} = 488 nm, λ_{em} = 500–600 nm, and Mito-Tracker Green imaging signal, λ_{ex} = 488 nm, λ_{em} = 650–750 nm, scale bar: 10 μm.

under physiological conditions.

To further demonstrate the pH specificity of SHD-SiRho, we conducted selectivity studies to explore its response toward various potential biologically relevant substances. The results, presented in Fig. S5, indicated tenuous changes in SHD-SiRho absorbance intensity when exposed to common reactive oxygen species, metal ions, and amino acids, highlighting its good selectivity. Additionally, PA selectivity studies (Figs. S6 and S7) further confirmed the robust anti-interference capability of SHD-SiRho. The PA detection ability of SHD-SiRho was then tested. Considering the characteristics of the probe's *UV–vis* absorption spectrum, we measured the PA spectra of the probes in pH 4.0 and pH 8.0 phosphate buffer solutions (PBS) (Fig. 2B) and the PA intensities at 680 nm and 730 nm in different pH PBS buffered solutions in the range of 4.0–8.0, respectively. Subsequently, we obtained $PA_{680\ nm}$ and $PA_{730\ nm}$ images of SHD-SiRho after processing in with different pH values. As shown in Fig. 2A and C, the PA intensity at 680 nm remained relatively stable with the change of buffer solution pH, whereas the PA intensity at 730 nm increased with the increase of buffer solution pH. Interestingly, the ratio of PA signal at 730 nm/680 nm showed good pH dependence in the range of 4.0–8.0 (Fig. 2D), which could be applicable to ratiometric PA imaging for detecting mitophagy microenvironment.

After obtaining the absorption and fluorescence emission spectra of SHD-SiRho, to enhance the reliability of the successful construction of this conclusion, and to illustrate the ability of the probe for in vivo fluorescence imaging, we carried out repones test in the 96-well plates using small animal imaging system. The SHD-SiRho probe was tested in different pH PBS buffered solutions. Three parallel samples of the same pH were sequentially added to a 96-well plate in a volume of 200 μL, followed by ICG (750–800 nm) and Cy5.5 (650–700 nm) dual-channel imaging. Fig. 2E and F showed fluorescence images of Cy5.5 and ICG channels, respectively. Fig. 2G displayed the data presentation in Fig. 2E and F. The obtained results revealed that the fluorescence intensity received in the Cy5.5 channel remained nearly unchanged, while the fluorescence detected in the ICG channel gradually increased with the increment of the pH. This observation aligns well with the measured fluorescence emission spectra. Fig. 2H demonstrates a pronounced pH sensitivity in the fluorescence signal intensity ratio of the ICG channel to the Cy5.5 channel within the pH range of 4.0–8.0. Furthermore, the fluorescence signal intensity ratio also displayed an incremental trend with increasing pH. These findings further confirmed the successful construction of SHD-SiRho as an internal reference fluorescent/PA probe. Notably, since the emission peaks of the probe in the ICG and

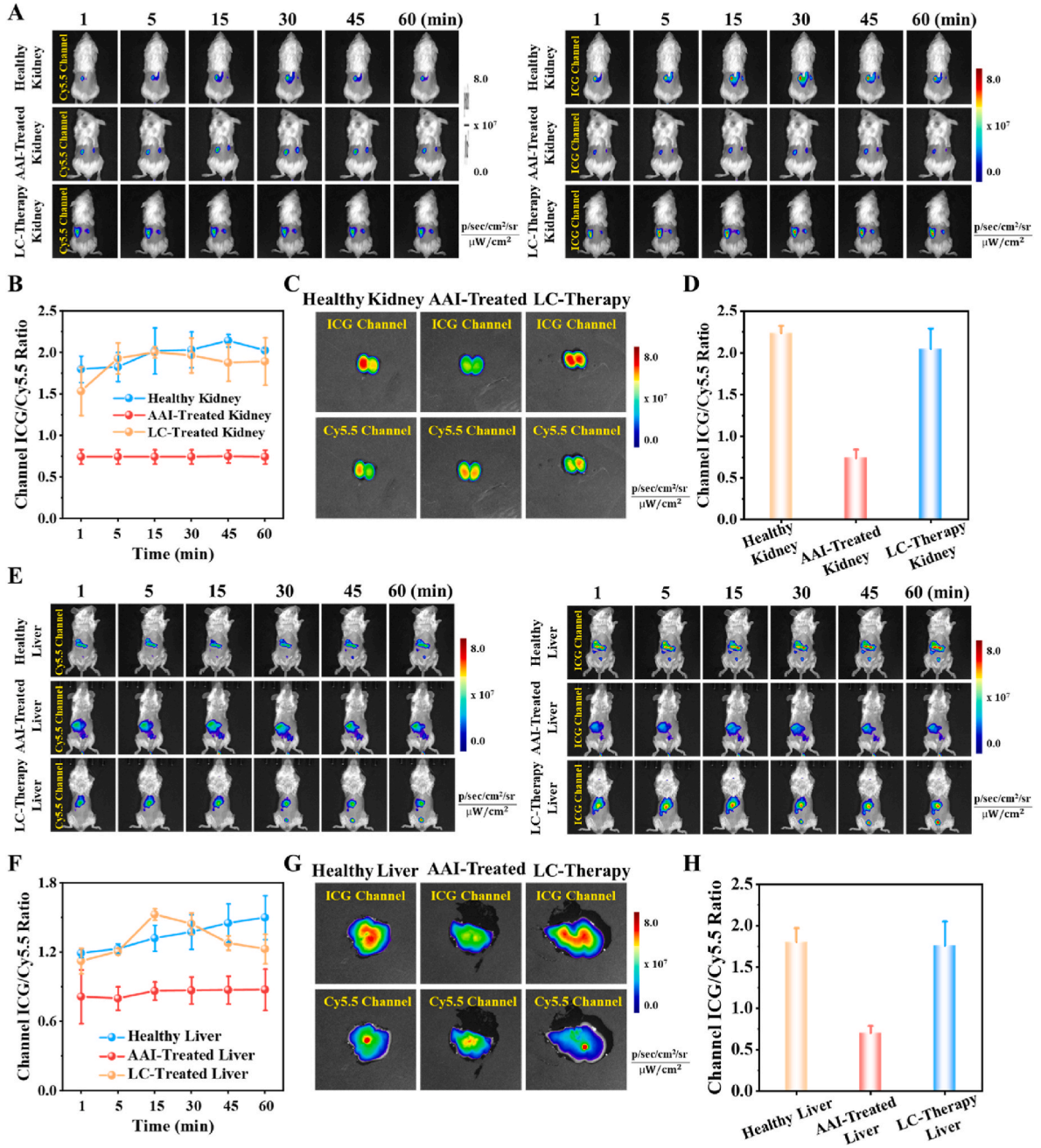

Fig. 5. In vivo fluorescence imaging of mitochondrial acidification in mice kidneys and livers, which were treated with DPBS, 200 μM AAI, and 200 μM AAI together with 1 mM LC for 24 h, respectively, with SHD-SiRho (50 μM, 25 μL in saline/DMSO, v/v = 4:1, pH 7.4). (A) In vivo dual-channel fluorescent imaging of kidneys after i. v. injecting of probe; (B) the ratio of relative fluorescence intensity in ICG/Cy5.5 channel in A; (C) Ex vivo dual-channel fluorescent imaging of mouse kidneys after i. v. injecting of probe for 30 min; (D) the ratio of relative fluorescence intensity in ICG/Cy5.5 channel in C. (E) In vivo dual-channel fluorescent imaging of livers after i. v. injecting of probe; (F) the ratio of relative fluorescence intensity in ICG/Cy5.5 channel in E; (G) Ex vivo dual-channel fluorescent imaging of mouse livers after i. v. injecting of probe for 30 min; (H) the ratio of relative fluorescence intensity in ICG/Cy5.5 channel in F. λ_{ex} = 640 nm, λ_{em} = 650–700 nm and 750–800 nm for fluorescent imaging.

Cy5.5 channels do not interfere with each other, the SHD-SiRho probe holds promising potential for live small animal ratio fluorescence imaging.

Subcellular localization of SHD-SiRho. Prior to conducting cell imaging experiments, the cytotoxicity of the SHD-SiRho probe on HK-2 cells was assessed using the MTS colorimetric assay. Fig. S8 demonstrates that after a 2 h co-incubation of HK-2 cells with different concentrations of SHD-SiRho, cell viability remained high, indicating low toxicity and favorable biocompatibility of the probe. However, for monitoring the mitophagy, considering that the probe may be require to co-incubate with HK-2 cells for a few hours, we also studied the influence of SHD-SiRho to cell activity after pretreated the cells with it for 6 h. The results exhibited that the probe after co-incubation for 6 h, induced obvious toxicity at a high concentration of 10 μM, which is mainly due to the depolarizing mitochondria membrane potential [55]. Thus, a probe concentration of 2.5 μM was selected for subsequent cell imaging experiments. Then, the co-localization study revealed that SHD-SiRho could be located in mitochondria with a high Pearson correlation coefficient. The lipophilic cationic module of SHD-SiRho supports its effective mitochondrial targeting in HeLa, L-O2 and HK-2 cells.

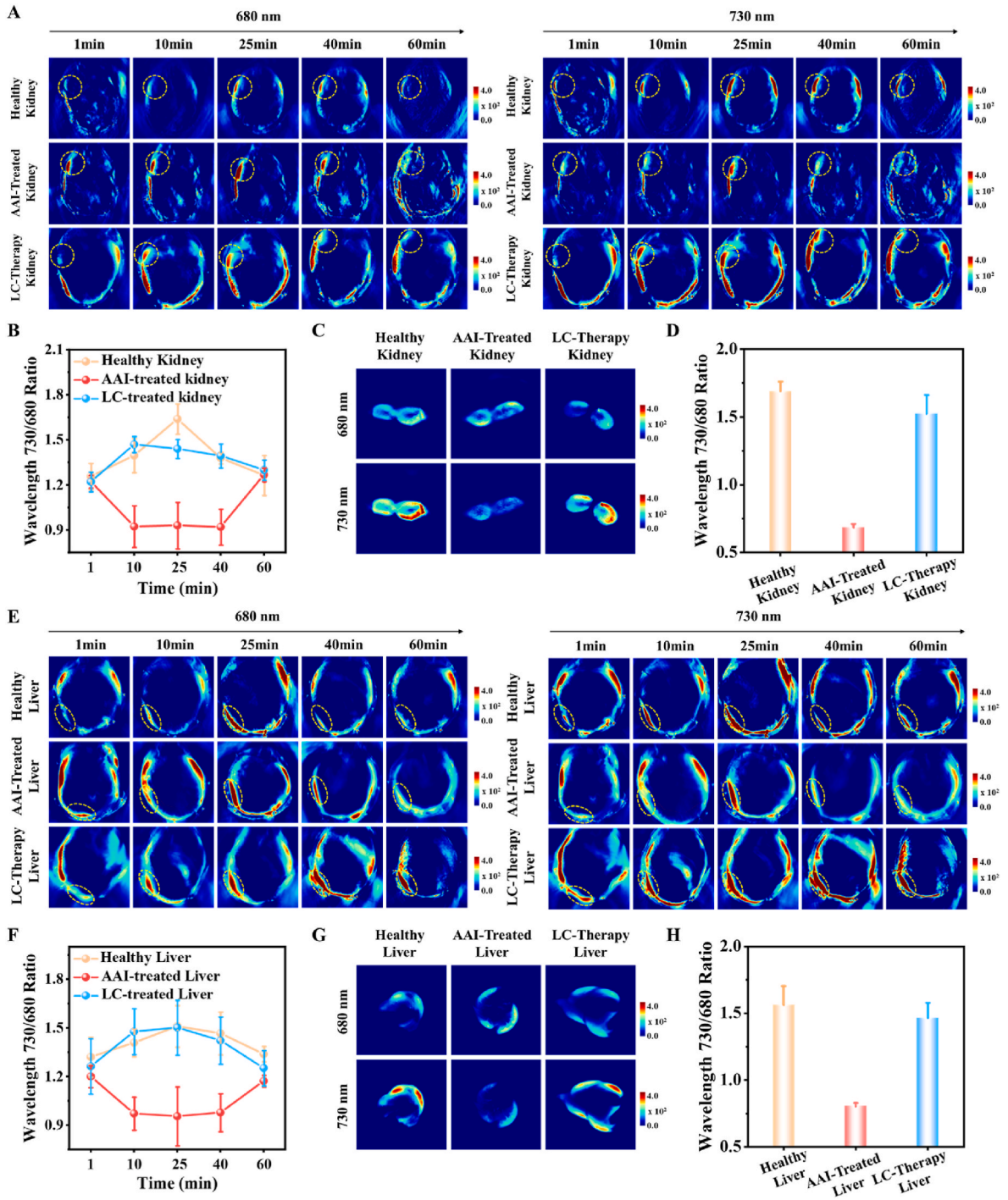

Fig. 6. *In vivo* PA imaging of mitochondrial acidification in kidneys and livers, which were treated with DPBS, 200 μM AAI, and 200 μM AAI together with 1 mM LC for 24 h, respectively, with SHD-SiRho (50 μM, 25 μL in DPBS/DMSO, v/v = 9:1, pH 7.4). (A) In vivo dual-channel PA imaging of kidneys after i. v. injecting of probe; (B) the ratio of relative PA signal intensity in $PA_{730\ nm}/PA_{680\ nm}$ channel in A; (C) Ex vivo dual-channel PA imaging of mouse kidneys after i. v. injecting of probe for 30 min; (D) the ratio of relative PA signal intensity in $PA_{730\ nm}/PA_{680\ nm}$ channel in C. (E) In vivo dual-channel PA imaging of livers after i. v. injecting of probe; (F) the ratio of relative PA signal intensity in $PA_{730\ nm}/PA_{680\ nm}$ channel in E; (G) Ex vivo dual-channel PA imaging of mouse kidneys after i. v. injecting of probe for 30 min; (H) the ratio of relative PA signal intensity in $PA_{730\ nm}/PA_{680\ nm}$ channel in G. λ_{ex} = 680 nm and 730 nm for PA imaging.

In sharp contrast, a slight overlap was observed between the fluorescence from the Lyso-Tracker channel and the SiRho channel. Therefore, the probe SHD-SiRho accumulates predominantly in the mitochondria, which can be applied to tracking mitophagy.

Fluorescence imaging of mitochondrial acidification in living cells. To validate the suitability of the SHD-SiRho probe for detecting mitophagy processes in living cells, we firstly established a hypoxia model, in which an extremely hypoxic condition (~0.1 % O_2) was constructed with an AnaeroPack in a clear container, and cultured HeLa cells in a container with SHD-SiRho for different time to trigger mitophagy. With the prolongation of hypoxia, the fluorescence emission intensity in the green channel (660–700 nm) kept bright while the fluorescence in the red channel (720–780 nm) decreased (Fig. S9). This observation suggests a reduction in mitochondrial pH during

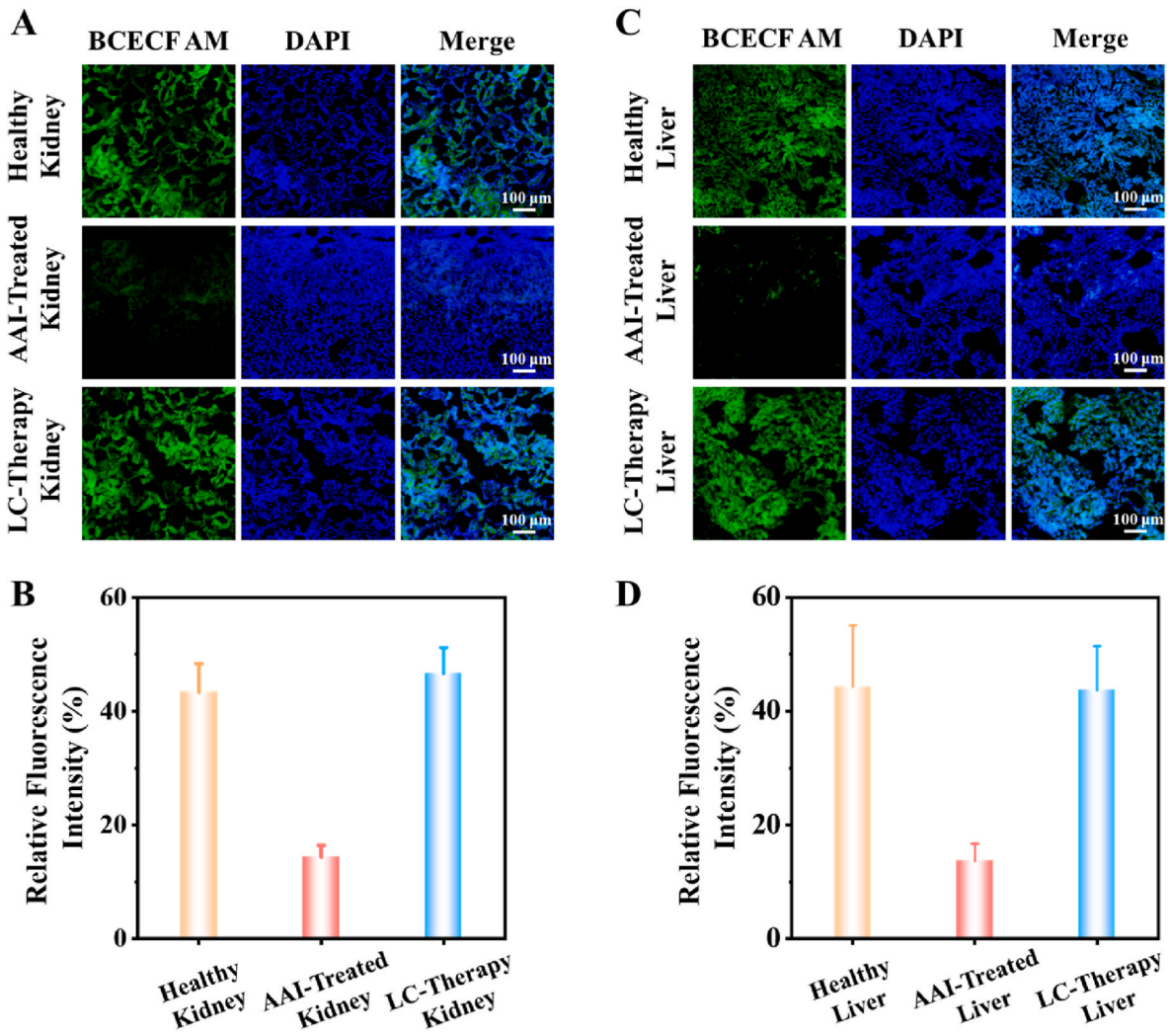

Fig. 7. Imaging of renal tissues separated and sectioned from mice, which were treated with DPBS, 200 μM AAI, and 200 μM AAI together with 1 mM LC for 24 h, respectively. Fluorescence imaging of (A) renal tissues and hepatic tissue (C), which were stained with 10 μM BCECF-AM and 10 μM DAPI for 30 min; (B) Relative fluorescence intensity in BCECF-AM channel in A; (D) Relative fluorescence intensity in BCECF-AM channel in C. λ_{ex} = 488 nm, λ_{em} = 500–550 nm for fluorescent tissues imaging.

mitophagy, leading to a weakened fluorescence intensity in the SHD component of the probe. Then, we studied the subcellular organelle distribution of SHD-SiRho in hypoxia-induced mitophagy by colocalization experiment. As displayed in Fig. 3C and D, the HeLa cells after coincubation with the probe for 6 h under 0.1 % O_2 hypoxic condition, the green signal from the SiRho showed large overlap with the LysoTracker® Green (Green and blue overlap to obtain cyan), and the red signal from the SHD exhibited completed overlap with LysoTracker® Green (red and blue overlap to obtain pink). These results confirmed that SHD-SiRho was able to monitor the mitochondrial acidification during mitophagy and could remain in mitochondria that undergo autophagy. Subsequently, fluorescence imaging experiments were conducted to investigate mitochondrial autophagy in HK-2 cells induced by AAI. As depicted in Fig. 4, the fluorescence intensity of the SiRho channel remained largely unchanged in the fluorescence imaging map of HK-2. In contrast, the significantly decreased fluorescence intensity of the SHD channel in HK-2 was observed at higher concentrations of AAI. While, the fluorescent signal of SHD channel was restored after the HK-2 cells co-incubated with L-carnitine (LC, an antioxidant), possibly because that the AAI-induced oxidative stress will be suppressed when HK-2 cells were treated with antioxidant [56]. We also studied the subcellular organelle distribution of SHD-SiRho in AAI-induced mitophagy by colocalization experiment (Fig. 4E and F), with the results verifying that the probe mainly remained in autophagy mitochondria. The fluorescence intensity and ratio of green channel (SiRho imaging signal) and red channel (SHD imaging signal) from HK-2 cells in each group were measured (Fig. 4G and H). The relative fluorescence signal ratio of SHD/SiRho channel in HK-2 cells without AAI-induced mitochondrial acidification and HK-2 cells incubated with 10 μM AAI and 100 μM LC were parallel and significantly higher than that of HK-2 cells incubated with 5 μM or 10 μM AAI (Fig. 4I). These results support the sensitivity and stability of ratiometric imaging effect of SHD-SiRho in cellular mitochondrial acidification. The occurrence of mitophagy in HK-2 cells was further verified by an upregulated protein expression of LC3-II operating the western blotting experiment (Fig. S10). These findings confirm the direct impact of AAI concentration on the extent of mitochondrial autophagy. The above results show that the probe SHD-SiRho can be used to monitor the mitochondrial process in HK-2 cells and can distinguish different mitophagy processes. Besides, the AAI may also induce hepatotoxicity, to this end, we also investigated the occurrence of mitophagy in LO-2 cells, with similar results indicating that AAI-induced hepatotoxicity may also associate with oxidative stress-aroused mitophagy (Fig. S11) [57].

Fluorescent/PA dual-modal imaging of mitochondrial acidification in living mice. To determine the optimal point of time for signal enrichment in the kidneys and achieve optimal imaging effect, the

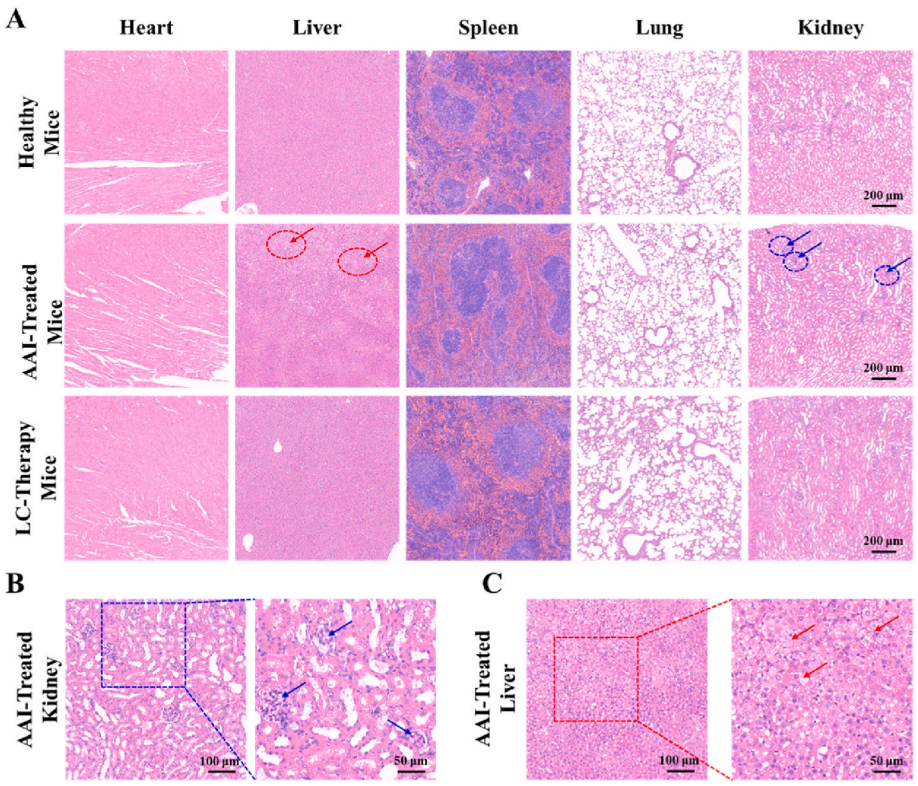

Fig. 8. (A) Representative photomicrographs of H&E staining of main organs from mice in groups. Red circles and arrows: injured hepatic tissue. Blue circles and arrows: injured renal glomerulus. (B) Representative photomicrographs of H&E staining of AAI-Treated kidney. Blue arrows: injured renal glomerulus. Scale bar: 100 μm and 50 μm. (C) Representative photomicrographs of H&E staining of AAI-Treated liver. Red arrows: injured hepatic tissue. Scale bar: 100 μm and 50 μm.

fluorescence imaging at different time nodes after the probe injection was investigated. Fig. S12 illustrated that the probe rapidly accumulated at the kidney site within 15 min of administration, and the signal intensity showed slight decrease at time point of 30 min, indicating the good kidney targeting ability. Then, the mice were dived into three group, treated with DPBS, 200 μM AAI, and 200 μM AAI together with 1 mM LC, respectively, for two weeks with five injections per week. Then, probe SHD-SiRho were tail vein injected and the in vivo fluorescence imaging were carried out. As displayed in Fig. 5A, both the blank group and AAI-treated group exhibited intense fluorescence in the Cy5.5 channels (signal came from the SiRho), while the fluorescence intensity in the ICG channel (signal came from the SHD) was notably lower compared to the blank group. While, when the mice were pretreated with 200 μM AAI and 1 mM LC together, the fluorescence intensity in the Cy5.5 channel showed similar to the above two groups, but the fluorescence intensity in the ICG channel displayed recovery compared to the only 200 μM AAI treated group. Subsequently, by calculating the ratio value of ICG channel to Cy5.5 channel using the collected signals, we observed that the ratio value was significantly lower in AAI-treated mice than in healthy mice and LC-therapy mice (Fig. 5B and Fig. S13), which clear indicated that mitochondrial acidification occurred in the AAI-treated mice, and LC could protect the kidneys from AAI-induced renal injury. The ex vivo imaging of the kidneys were also performed with the results displayed in Fig. 5C. The ex vivo imaging result also verified the low ICG/Cy5.5 ratio of the AAI-treated group compared to healthy group and LC-therapy group (Fig. 5D). Therefore, the intensity of the ratio signal can serve as an indicator to assess renal cell mitochondrial acidification in mice with renal injury.

The AAI-induced liver injury was also studied as a large portion of the probe are preferentially enriched in the liver. As shown in Fig. 5E, similar results could be observed in AAI-induced liver injury, i.e, both the Control group, AAI-treated livers and LC-Therapy livers exhibited intense fluorescence in the Cy5.5 channels, while the fluorescence intensity of AAI-treated livers in the ICG channels was notably lower compared to other groups, thus the ratiometric fluorescent signals of AAI-treated livers was decreased during the observation period (Fig. 5F). These experimental findings are in principle consistent with previous research results based on proteomics [7,8]. Similarly, the corresponding ratiometric fluorescence signal of the ex vivo liver was also significantly reduced in the AAI-treated group compared to healthy group and LC-Therapy group (Fig. 5G and H). The above results demonstrated that SHD-SiRho were capable of NIR fluorescent/PA bimodal imaging of mitochondrial acidification in AAI-induced kidney and liver injury, with an interesting experimental finding that joint use of LC could mitigate the mitophagy in AAI-induced kidney and liver injury.

The fluorescence is only one-dimensional imaging, and fluorescent imaging is susceptible to tissue depth. The PA imaging can achieve higher penetration depth and spatial resolution than fluorescence imaging. By complementing the advantages of the fluorescent/PA bimodal imaging and verifying their imaging results with each other, more comprehensive information can be provided for in vivo mitophagy. Therefore, the PA imaging was also adopted to visualize mitochondrial acidification in vivo by the equal method. As shown in Fig. 6, the results of the PA imaging experiment for SHD-SiRho also showed the accordant trend as the fluorescence imaging experiment. Comparative analysis of the ratio in each group indicated that the probe can effectively monitor mitochondrial acidification in mice with renal injury. Comparative analysis of ratiometric photoacoustic signals in each group indicated that the probe can effectively monitor mitochondrial acidification in mice with renal and hepatic injury. In details, the photoacoustic imaging of kidneys and livers in healthy mice, AAI-treated mice and LC-therapy mice was executed at different time nodes after the probe injection (Fig. 6A and E). And the ratiometric photoacoustic signals of $PA_{730\ nm}$/$PA_{680\ nm}$ in AAI-treated kidneys (Fig. 6B) and AAI-treated livers (Fig. 6E) were notably lower compared to other groups. Notably, the

corresponding ratiometric fluorescence signals of the ex vivo kidneys (Fig. 6C and D) and livers (Fig. 6G and H) were also significantly reduced in the AAI-treated group compared to healthy group and LC-Therapy group.

In addition, after in vivo imaging experiment, the mice were dissected and prime organs were separated and sectioned for tissues fluorescent imaging and hematoxylin-eosin (H&E) staining. We used BCECF-AM, a fluorescent pH indicator that penetrates the cell membrane and can display intense fluorescence under alkaline environment, to detect the pH of renal tissue. As shown in Fig. 7A, the fluorescence intensity of BCECF-AM in the healthy and LC-therapy Treated kidneys and LC-therapy Treated livers were intense, while negligible in the AAI-Treated kidneys (Fig. 7A and B) and AAI-Treated livers (Fig. 7C and D). The H&E staining of main organs, including heart, liver, spleen, lung and kidney, displayed that the liver and kidney of mice treated with AAI showed obvious damage, including large areas of necrosis and edema in the liver (red circles and arrows); necrosis in the glomeruli (blue circles and arrows); no significant organ damage was observed in the LC-cotreatment mice; and the probes exhibited no significant toxicological effects on the organs of healthy mice (Fig. 8).

3. Conclusion

In conclusion, we successfully developed the SHD-SiRho probe, an internal reference ratio-type near-infrared probe, for in vivo monitoring of AAI-induced mitochondrial acidification. The probe exhibited remarkable sensitivity and specificity to changes in both solution and intracellular pH, and demonstrated a reversible response within the physiological pH range. As the pH decreased, the fluorescence at 680 nm remained nearly unchanged, while the fluorescence at 780 nm exhibited obvious variations. Similarly, the absorbance at 680 nm remained nearly unchanged, while the absorbance at 730 nm exhibited obvious variations. These changes in dual signals enable ratiometric NIR fluorescent/PA dual-modal imaging. Furthermore, colocalization studies of the probe indicated its effective targeting of mitochondria. Notably, imaging of HK-2 cells in the AAI-induced renal injury and hepatic injury model revealed that the probe exhibited mitochondrial enrichment and demonstrated sensitivity in detecting mitochondrial acidification during mitophagy. Moreover, the probe could quickly accumulate in kidney and liver, successfully applied for fluorescent/PA dual-modal imaging of AAI-induced mitophagy in vivo in a ratiometric manner by generating different fluorescence signals. Therefore, this work provides a great tool for in vivo noninvasive, real-time, semi-quantitative pH imaging, particularly useful for the investigation of kidney microenvironment, as well as for the prognosis of drug induced renal injury.

CRediT authorship contribution statement

Li Xu: Writing – original draft, Formal analysis, Data curation. **Li Chen:** Methodology, Investigation. **Hongwen Liu:** Writing – review & editing, Supervision, Project administration. **Xingwang Chen:** Writing – original draft, Visualization, Software. **Shenghang Zhang:** Supervision, Project administration, Funding acquisition.

Declaration of competing interest

The authors declare that they have no known competing financial interests or personal relationships that could have appeared to influence the work reported in this paper.

Data availability

Data will be made available on request.

Acknowledgements

This work was supported by National Natural Science Foundation of China (Grants 22104036), Cooperative Project with Foreign Investigator, Natural Science Foundation of Fujian Province of China (2023I0029), Joint Funds for the innovation of science and Technology, Fujian province (2023Y9267), Fund Raised for the Fujian Clinical Research Center for Aptamer-based Precision Testing (2021Y2017), Fund from Management Project of Fujian University of Traditional Chinese Medicine (XB2023182). The Open Research Fund of the School of Chemistry and Chemical Engineering, Henan Normal University (2024Y04).

Appendix A. Supplementary data

Supplementary data to this article can be found online at https://doi.org/10.1016/j.mtbio.2024.101240.

References

[1] E.E. Anger, F. Yu, J. Li, Aristolochic acid-induced nephrotoxicity: molecular mechanisms and potential protective approaches, Int. J. Mol. Sci. 21 (2020) 32050524, https://doi.org/10.3390/ijms21031157.
[2] Q. Zhou, J. Pei, J. Poon, A.Y. Lau, L. Zhang, Y. Wang, et al., Worldwide research trends on aristolochic acids (1957-2017): suggestions for researchers, PLoS One 14 (2019) e0216135, https://doi.org/10.1371/journal.pone.0216135.
[3] C.C. Yang, C.T. Wu, L.P. Chen, K.Y. Hung, S.H. Liu, C.K. Chiang, Autophagy induction promotes aristolochic acid-I-induced renal injury in vivo and in vitro, Toxicology 312 (2013) 63–73, https://doi.org/10.1016/j.tox.2013.07.017.
[4] Y. Lu, Z. Li, S. Zhang, T. Zhang, Y. Liu, L. Zhang, Cellular mitophagy: mechanism, roles in diseases and small molecule pharmacological regulation, Theranostics 13 (2023) 736–766, https://doi.org/10.7150/thno.79876.
[5] R.J. Youle, D.P. Narendra, Mechanisms of mitophagy, Nat. Rev. Mol. Cell Bio. 12 (2011) 9–14, https://doi.org/10.1038/nrm3028.
[6] D.A. Kubli, Å.B. Gustafsson, Mitochondria and mitophagy, Circ. Res. 111 (2012) 1208–1221, https://doi.org/10.1161/CIRCRESAHA.112.265819.
[7] Y.L. Man, H.L. Rui, Y.P. Chen, G.Q. Wang, L.J. Sun, H. Cheng, Aristolochic acid-induced autophagy promotes epithelial-to-myofibroblast transition in human renal proximal tubule epithelial cells, evidence-based complementary and alternative medicine, eCAM 2017 (2017) 9596256, https://doi.org/10.1155/2017/9596256.
[8] C. Jin, X. Miao, Y. Zhong, J. Han, Q. Liu, J. Zhu, et al., The renoprotective effect of diosgenin on aristolochic acid I-induced renal injury in rats: impact on apoptosis, mitochondrial dynamics and autophagy, Food Func 11 (2020) 7456–7467, https://doi.org/10.1039/D0FO00401D.
[9] X. Li, X. Liang, J. Yin, W. Lin, Organic fluorescent probes for monitoring autophagy in living cells, Chem. Soc. Rev. 50 (2021) 102–119, https://doi.org/10.1039/D0CS00896F.
[10] N.J. Dolman, K.M. Chambers, B. Mandavilli, R.H. Batchelor, M.S. Janes, Tools and techniques to measure mitophagy using fluorescence microscopy, Autophagy 9 (2013) 1653–1662, https://doi.org/10.4161/auto.24001.
[11] H.-W. Liu, L. Chen, C. Xu, Z. Li, H. Zhang, X.-B. Zhang, et al., Recent progresses in small-molecule enzymatic fluorescent probes for cancer imaging, Chem. Soc. Rev. 47 (2018) 7140–7180, https://doi.org/10.1039/C7CS00862G.
[12] M. Kim, C. Chen, Z. Yaari, R. Frederiksen, E. Randall, J. Wollowitz, et al., Nanosensor-based monitoring of autophagy-associated lysosomal acidification in vivo, Nature Chem. Bio. 19 (2023) 1448–1457, https://doi.org/10.1038/s41589-023-01364-9.
[13] P. Wu, D.J. Siegwart, H. Xiong, Recent advances in the targeted fluorescent probes for the detection of metastatic bone cancer, Sci. China Chem. 64 (2021) 1283–1296, https://doi.org/10.1007/s11426-021-9990-x.
[14] H.-H. Han, H. Tian, Y. Zang, A.C. Sedgwick, J. Li, J.L. Sessler, et al., Small-molecule fluorescence-based probes for interrogating major organ diseases, Chem. Soc. Rev. 50 (2021) 9391–9429, https://doi.org/10.1039/D0CS01183E.
[15] X.-P. Fan, J. Huang, T.-B. Ren, L. Yuan, X.-B. Zhang, De novo design of activatable photoacoustic/fluorescent probes for imaging acute lung injury in vivo, Anal. Chem. 95 (2023) 1566–1573, https://doi.org/10.1021/acs.analchem.2c04642.
[16] C.N. Loynachan, A.P. Soleimany, J.S. Dudani, Y. Lin, A. Najer, A. Bekdemir, et al., Renal clearable catalytic gold nanoclusters for in vivo disease monitoring, Nature Nanotech 14 (2019) 883–890, https://doi.org/10.1038/s41565-019-0527-6.
[17] Y. Li, G. Wang, T. Wang, C. Li, X. Zhang, J. Li, et al., PEGylated gambogic acid nanoparticles enable efficient renal-targeted treatment of acute kidney injury, Nano Lett. 23 (2023) 5641–5647, https://doi.org/10.1021/acs.nanolett.3c01235.
[18] X. Jiang, B. Du, S. Tang, J.-T. Hsieh, J. Zheng, Photoacoustic imaging of nanoparticle transport in the kidneys at high temporal resolution, Angew. Chem. Int. Ed. 58 (2019) 5994–6000, https://doi.org/10.1002/anie.201901525.
[19] H. Soo Choi, W. Liu, P. Misra, E. Tanaka, J.P. Zimmer, B. Itty Ipe, et al., Renal clearance of quantum dots, Nature Biotech 25 (2007) 1165–1170, https://doi.org/10.1038/nbt1340.

[20] Y. Chen, P. Pei, Z. Lei, X. Zhang, D. Yin, F. Zhang, A promising NIR-II fluorescent sensor for peptide-mediated long-term monitoring of kidney dysfunction, Angew. Chem. Int. Ed. 60 (2021) 15809–15815, https://doi.org/10.1002/anie.202103071.
[21] J. Huang, K. Pu, Near-infrared fluorescent molecular probes for imaging and diagnosis of nephro-urological diseases, Chem. Sci. 12 (2021) 3379–3392, https://doi.org/10.1039/D0SC02925D.
[22] H.-W. An, D. Hou, R. Zheng, M.-D. Wang, X.-Z. Zeng, W.-Y. Xiao, et al., A near-infrared peptide probe with tumor-specific excretion-retarded effect for image-guided surgery of renal cell carcinoma, ACS Nano 14 (2020) 927–936, https://doi.org/10.1021/acsnano.9b08209.
[23] J. Huang, Y. Jiang, J. Li, S. He, J. Huang, K. Pu, A renal-clearable macromolecular reporter for near-infrared fluorescence imaging of bladder cancer, Angew. Chem. Int. Ed. 59 (2020) 4415–4420, https://doi.org/10.1002/anie.201911859.
[24] B. Du, Y. Chong, X. Jiang, M. Yu, U.-G. Lo, A. Dang, et al., Hyperfluorescence imaging of kidney cancer enabled by renal secretion pathway dependent efflux transport, Angew. Chem. Int. Ed. 60 (2021) 351–359, https://doi.org/10.1002/anie.202010187.
[25] Z. Li, L. Xu, J.-Y. Li, L. Lei, P.-Z. Liang, Q. Wu, et al., Superoxide anion-mediated afterglow mechanism-based water-soluble zwitterion dye achieving renal-failure mice detection, J. Am. Chem. Soc. 145 (2023) 26736–26746, https://doi.org/10.1021/jacs.3c08579.
[26] S.L. Samodelov, G.A. Kullak-Ublick, Z. Gai, M. Visentin, Organic cation transporters in human physiology, pharmacology, and toxicology, Int. J. Mol. Sci. 21 (2020) 7890, https://doi.org/10.3390/ijms21217890.
[27] Y. Urakami, M. Okuda, H. Saito, K. Inui, Hormonal regulation of organic cation transporter OCT2 expression in rat kidney, FEBS Lett. 473 (2000) 173–176, https://doi.org/10.1016/S0014-5793(00)01525-8.
[28] Y. Urakami, N. Nakamura, K. Takahashi, M. Okuda, H. Saito, Y. Hashimoto, et al., Gender differences in expression of organic cation transporter OCT2 in rat kidney, FEBS Lett. 461 (1999) 339–342, https://doi.org/10.1016/S0014-5793(99)01491-X.
[29] M. Li, S. Long, Y. Kang, L. Guo, J. Wang, J. Fan, et al., De novo design of phototheranostic sensitizers based on structure-inherent targeting for enhanced cancer ablation, J. Am. Chem. Soc. 140 (2018) 15820–15826, https://doi.org/10.1021/jacs.8b09117.
[30] M. Li, T. Xiong, J. Du, R. Tian, M. Xiao, L. Guo, et al., Superoxide radical photogenerator with amplification effect: surmounting the achilles' heels of photodynamic oncotherapy, J. Am. Chem. Soc. 141 (2019) 2695–2702, https://doi.org/10.1021/jacs.8b13141.
[31] T. Fukuda, S. Yokomizo, S. Casa, H. Monaco, S. Manganiello, H. Wang, et al., Fast and durable intraoperative near-infrared imaging of ovarian cancer using ultrabright squaraine fluorophores, Angew. Chem. Int. Ed. 61 (2022) e202117330, https://doi.org/10.1002/anie.202117330.
[32] T. Ludwig, C. Riethmüller, M. Gekle, G. Schwerdt, H. Oberleithner, Nephrotoxicity of platinum complexes is related to basolateral organic cation transport, Kidney Inter 66 (2004) 196–202, https://doi.org/10.1111/j.1523-1755.2004.00720.x.
[33] Y. Wen, N. Jing, F. Huo, C. Yin, Recent progress of organic small molecule-based fluorescent probes for intracellular pH sensing, Analyst 146 (2021) 7450–7463, https://doi.org/10.1039/D1AN01621K.
[34] J. Ma, R. Sun, K. Xia, Q. Xia, Y. Liu, X. Zhang, Design and application of fluorescent probes to detect cellular physical microenvironments, Chem. Rev. 124 (2024) 1738–1861, https://doi.org/10.1021/acs.chemrev.3c00573.
[35] Y. Hou, J. Zhou, Z. Gao, X. Sun, C. Liu, D. Shangguan, et al., Protease-Activated ratiometric fluorescent probe for pH mapping of malignant tumors, ACS Nano 9 (2015) 3199–3205, https://doi.org/10.1021/acsnano.5b00276.
[36] T. Ma, Y. Hou, J. Zeng, C. Liu, P. Zhang, L. Jing, et al., Dual-ratiometric target-triggered fluorescent probe for simultaneous quantitative visualization of tumor microenvironment protease activity and pH in vivo, J. Am. Chem. Soc. 140 (2018) 211–218, https://doi.org/10.1021/jacs.7b08900.
[37] Q. Chen, X. Liu, J. Chen, J. Zeng, Z. Cheng, Z. Liu, A self-assembled albumin-based nanoprobe for in vivo ratiometric photoacoustic pH imaging, Adv. Mater. 27 (2015) 6820–6827, https://doi.org/10.1002/adma.201503194.
[38] X. Zhang, Z.-W. Li, Y. Wu, X. Ge, L. Su, H. Feng, et al., Highly controlled janus organic-inorganic nanocomposite as a versatile photoacoustic platform, Angew. Chem. Int. Ed. 60 (2021) 17647–17653, https://doi.org/10.1002/anie.202105207.
[39] Z. Wang, L. Wang, H. Bian, Z. Huang, X. Zhang, Y. Xiao, Outer surface-labeled bacteria as live sens. Accurately quantitating interfacial pH: a smart technique for antimicrobial resistance, ACS Nano 16 (2022) 18344–18354, https://doi.org/10.1021/acsnano.2c06226.
[40] Y. Liu, L. Teng, L. Chen, H. Ma, H.-W. Liu, X.-B. Zhang, Engineering of a near-infrared fluorescent probe for real-time simultaneous visualization of intracellular hypoxia and induced mitophagy, Chem. Sci. 9 (2018) 5347–5353, https://doi.org/10.1039/C8SC01684D.
[41] Y. Liu, L. Teng, B. Yin, H. Meng, X. Yin, S. Huan, et al., Chemical design of activatable photoacoustic probes for precise biomedical applications, Chem. Rev. 122 (2022) 6850–6918, https://doi.org/10.1021/acs.chemrev.1c00875.
[42] Y. Ma, L. Liu, Z. Ye, L. Xu, Y. Li, S. Liu, et al., Engineering of cyanine-based nanoplatform with tunable response toward reactive species for ratiometric NIR-II fluorescent imaging in mice, Sci. Bull. 68 (2023) 2382–2390, https://doi.org/10.1016/j.scib.2023.08.041.
[43] Y. Zhao, L. Li, Q. Ye, Y. Gong, R. Yang, H. Liu, Reaction-Activated disassembly of the NIR-II probe enables fast detection and ratiometric photoacoustic imaging of glutathione in vivo, Anal. Chem. 95 (2023) 14043–14051, https://doi.org/10.1021/acs.analchem.3c02664.
[44] Z. Jiang, C. Zhang, Q. Sun, X. Wang, Y. Chen, W. He, et al., A NIR-II photoacoustic probe for high spatial quantitative imaging of tumor nitric oxide in vivo, Angew. Chem. Int. Ed. 63 (2024) e202320072, https://doi.org/10.1002/anie.202320072.
[45] X.-P. Fan, W. Yang, T.-B. Ren, S. Xu, X.-Y. Gong, X.-B. Zhang, L. Yuan, Engineering a ratiometric photoacoustic probe with a hepatocyte-specific targeting ability for liver injury imaging, Anal. Chem. 94 (2) (2022) 1474–1481, https://doi.org/10.1021/acs.analchem.1c05026.
[46] W.-L. Jiang, Y. Li, W.-X. Wang, Y.-T. Zhao, J. Fei, C.-Y. Li, A hepatocyte-targeting near-infrared ratiometric fluorescent probe for monitoring peroxynitrite during drug-induced hepatotoxicity and its remediation, Chem. Commun. 55 (95) (2019) 14307–14310, https://doi.org/10.1039/C9CC07017F.
[47] W.-L. Jiang, W.-X. Wang, J. Liu, Y. Li, C.-Y. Li, A novel hepatocyte-targeting ratiometric fluorescent probe for imaging hydrogen peroxide in zebrafish, Sensors Actuat. B-Chem. 313 (2020) 128054, https://doi.org/10.1016/j.snb.2020.128054.
[48] Y. Zhang, X. Chen, Q. Yuan, Y. Bian, M. Li, Y. Wang, X. Gao, D. Su, Enzyme-activated near-infrared fluorogenic probe with high-efficiency intrahepatic targeting ability for visualization of drug-induced liver injury, Chem. Sci. 12 (44) (2021) 14855–14862, https://doi.org/10.1039/D1SC04825B.
[49] H.S. Choi, S.L. Gibbs, J.H. Lee, S.H. Kim, Y. Ashitate, F. Liu, H. Hyun, G. Park, Y. Xie, S. Bae, M. Henary, J.V. Frangioni, Targeted zwitterionic near-infrared fluorophores for improved optical imaging, Nature Biotechnol 31 (2) (2013) 148–153, https://doi.org/10.1038/nbt.2468.
[50] H. Hyun, M.H. Park, E.A. Owens, H. Wada, M. Henary, H.J.M. Handgraaf, A. L. Vahrmeijer, J.V. Frangioni, H.S. Choi, Structure-inherent targeting of near-infrared fluorophores for parathyroid and thyroid gland imaging, Nature Med 21 (2) (2015) 192–197, https://doi.org/10.1038/nm.3728.
[51] H.-W. Liu, H. Zhang, X. Lou, L. Teng, J. Yuan, L. Yuan, X.-B. Zhang, W. Tan, Imaging of peroxynitrite in drug-induced acute kidney injury with a near-infrared fluorescence and photoacoustic dual-modal molecular probe, Chem. Commun. 56 (58) (2020) 8103–8106, https://doi.org/10.1039/D0CC01621G.
[52] S. Zhang, H. Chen, L. Wang, X. Qin, B.P. Jiang, S.C. Ji, et al., A general approach to design dual ratiometric fluorescent and photoacoustic probes for quantitatively visualizing tumor hypoxia levels in vivo, Angew. Chem. Int. Ed. 61 (2022) e202107076, https://doi.org/10.1002/anie.202107076.
[53] Y. Koide, Y. Urano, K. Hanaoka, W. Piao, M. Kusakabe, N. Saito, et al., Development of NIR fluorescent dyes based on Si–rhodamine for in vivo imaging, J. Am. Chem. Soc. 134 (2012) 5029–5031, https://doi.org/10.1021/ja210375e.
[54] J.-N. Han, C. Zhong, M. Ge, S. Kuang, Z. Nie, Engineering fluorescent protein chromophores with an internal reference for high-fidelity ratiometric G4 imaging in living cells, Chem. Sci. 14 (2023) 4538–4548, https://doi.org/10.1039/D3SC00022B.
[55] C.-J. Zhang, Q. Hu, G. Feng, R. Zhang, Y. Yuan, X. Lu, et al., Image-guided combination chemotherapy and photodynamic therapy using a mitochondria-targeted molecular probe with aggregation-induced emission characteristics, Chem. Sci. 6 (2015) 4580–4586, https://doi.org/10.1039/C5SC00826C.
[56] Y. Lv, C. Dan, S. Dongdong, M. Chen, B.-C. Yin, L. Yuan, et al., Visualization of oxidative injury in the mouse kidney using selective superoxide anion fluorescent probes, Chem. Sci. 9 (2018) 7606–7613, https://doi.org/10.1039/C8SC03308K.
[57] Y. Wang, X. Ma, C. Zhou, Y. Jia, S. Liu, Z. Xiong, et al., Aristolochic acid induces mitochondrial apoptosis through oxidative stress in rats, leading to liver damage, Toxicol. Mech. Method. 31 (2021) 609–618, https://doi.org/10.1080/15376516.2021.1946229.